This is a repository copy of *The thermodynamics of calcite nucleation at organic interfaces: Classical vs. non-classical pathways*.

White Rose Research Online URL for this paper:
http://eprints.whiterose.ac.uk/86509/

Version: Accepted Version

Article:
Hu, Q., Nielsen, M.H., Freeman, C.L. et al. (8 more authors) (2012) The thermodynamics of calcite nucleation at organic interfaces: Classical vs. non-classical pathways. Faraday Discussions, 159. 509 - 523. ISSN 1359-6640

https://doi.org/10.1039/c2fd20124k

Reuse
Unless indicated otherwise, fulltext items are protected by copyright with all rights reserved. The copyright exception in section 29 of the Copyright, Designs and Patents Act 1988 allows the making of a single copy solely for the purpose of non-commercial research or private study within the limits of fair dealing. The publisher or other rights-holder may allow further reproduction and re-use of this version - refer to the White Rose Research Online record for this item. Where records identify the publisher as the copyright holder, users can verify any specific terms of use on the publisher's website.

Takedown
If you consider content in White Rose Research Online to be in breach of UK law, please notify us by emailing eprints@whiterose.ac.uk including the URL of the record and the reason for the withdrawal request.

eprints@whiterose.ac.uk
https://eprints.whiterose.ac.uk/

The thermodynamics of calcite nucleation at organic interfaces: Classical vs. non-classical pathways

Q. Hu[1,2,*], M.H. Nielsen[1,3,*], C.L. Freeman[4], L.M. Hamm[5], J. Tao[1], J.R.I Lee[6], T.Y.J. Han[6], U. Becker[2], J.H. Harding[4], P.M. Dove[5] and J.J. De Yoreo[1,#]

[1]Molecular Foundry, Lawrence Berkeley National Laboratory, Berkeley, CA 94720

[2]Department of Earth and Environmental Sciences, University of Michigan, Ann Arbor, MI 48109

[3]Department of Materials Science and Engineering, University of California, Berkeley, CA 94720

[4]Department of Materials Science and Engineering, University of Sheffield, Sheffield, U.K. S1 3JD

[5]Department of Geosciences, Virginia Tech, Blacksburg, VA 24061

[6]Physical and Life Sciences Directorate, Lawrence Livermore National Laboratory, Livermore, CA 94511

[*]These authors contributed equally

[#]Correspondence and request for materials should be directed to JJDY (jjdeyoreo@lbl.gov).

Nucleation in the natural world often occurs in the presence of organic interfaces. In mineralized tissues, a range of macromolecular matrices are found in contact with inorganic phases and are believed to direct mineral formation. In geochemical settings, mineral surfaces, which are often covered with organic or biological films, surround the volume within which nucleation occurs. In the classical picture of nucleation, the presence of such interfaces is expected to have a profound effect on nucleation rates, simply because they can reduce the interfacial free energy, which controls the height of the thermodynamic barrier to nucleation of the solid phase. However, the recent discovery of a nearly monodisperse population of calcium carbonate clusters — so called pre-nucleation clusters — and the many observations of amorphous precursor phases have called into question the applicability of classical descriptions. Here we use *in situ* observations of nucleation on organothiol self-assembled monolayers (SAMs) to explore the energetics and pathways of calcite nucleation at organic interfaces. We find that carboxyl SAM-directed nucleation is described well in purely classical terms through a reduction in the thermodynamic barrier due to decreased interfacial free energy. Moreover, the differences

in nucleation kinetics on odd and even chain-length carboxyl SAMs are attributable to relative differences in these energies. These differences arise from varying degrees of SAM order related to oxygen-oxygen interactions between SAM headgroups. In addition, amorphous particles formed prior to or during crystal nucleation do not grow and are not observed to act as precursors to the crystalline phase. Instead, calcite nucleates independently. These results imply that the recently proposed model of calcite formation as a non-classical process, one which proceeds via aggregation of stable pre-nucleation clusters that form an amorphous precursor from which the crystalline phase emerges, is not applicable to template-directed nucleation and does not provide a universal description of calcite formation.

1. Introduction

Macromolecular matrices play a key role in establishing the architectural complexity and mechanical properties of biominerals by directing the organization of the mineralized component.[1-3] The ability of the matrix to perform this function is determined by both its structural relationship with the incipient nucleus[4] and the changes to the energy landscape it imposes upon the mineralizing constituents.[5] A number of studies have explored the structural aspect,[1-4,6,7] but little is known about the energetic controls. Moreover, the recent discovery that calcium carbonate[8] and phosphate[4] solutions contain clusters prior to nucleation — i.e., pre-nucleation clusters — that seem to be stable relative to the free ions[8] combined with observations of non-equilibrium amorphous precursors in numerous biomineral[1,9,10] and biomimetic systems,[4,11,12] raises the question of whether the classical description[5] of nucleation dynamics is applicable to matrix-directed mineralization. This same question arises when considering mineral nucleation in geochemical settings where a surrounding mineral matrix, which is often coated with biofilms or other organic layers, is likely to influence nucleation kinetics. While these issues are difficult to address in the context of three-dimensional biological matrices or geological reservoirs, self-assembled monolayers (SAMs) of organothiols on noble metal surfaces, which can template mineral nucleation on distinct crystallographic planes with a high degree of specificity, offer an excellent 2D model.[12-16]

Here we use carboxyl- and hydroxyl-terminated SAMs to investigate the energetics and formation pathways during templated nucleation of $CaCO_3$. We first develop the basic

relationships between the rate of calcite nucleation and the supersaturation for three classes of free energy landscapes, including both size independent and size dependent excess free energies, as well as one in which local or global minima create a population of pre-nucleation clusters. We then utilize an *in situ* optical microscopy method to measure nucleation rates as a function of supersaturation on SAMs, from which we derive the effective interfacial energies for odd and even SAMs and compare the resulting free energy barriers for odd and even carboxyl-terminated SAMs to that expected for homogeneous nucleation in bulk solution. Molecular dynamics simulations are used to understand the structural source of the differences in nucleation rates observed for the odd and even SAMs. Finally a combination of *in situ* optical microscopy and atomic force microscopy (AFM) observations along with Raman and transmission electron microscopy (TEM) analyses are employed to follow the pathway of calcite formation on both the carboxyl- and hydroxyl-terminated SAMs.

Theoretical analysis shows that homogeneous nucleation of calcite is highly unlikely even at concentrations approaching the solubility limit of amorphous calcium carbonate (ACC). However, introduction of a size dependent interfacial energy, the introduction of low-energy surfaces and a population of metastable clusters can all significantly reduce the barrier. Based on our measurements of nucleation rates, we find that nucleation on carboxyl- terminated SAMs is described well in purely classical terms through a reduction in the thermodynamic barrier due to decreased interfacial free energy. Moreover, the differences in nucleation kinetics on carboxyl-terminated SAMs of odd and even parity — i.e., an odd number (11) vs. an even number (16) of carbons in the alkyl chain —are attributable to relative differences in these energies that arise from varying degrees of SAM order related to oxygen-oxygen interactions between SAM headgroups. In addition, amorphous particles observed to form prior to crystal nucleation on hydroxyl SAMs and sometimes during or after crystal nucleation on carboxyl SAMs — even well below the accepted bulk solubility limit for amorphous calcium carbonate (ACC) —do not grow and are not observed to be precursors to the crystalline phase. Instead, calcite appears to nucleate independently. We discuss how these results can be reconciled with the recently proposed non-classical picture of calcite formation that is based on aggregation of stable or metastable pre-nucleation clusters.[8,11]

2. Theoretical analysis of nucleation rates

In principle, the energetic effect of any surface on nucleation can be determined by measuring the dependence of nucleation rate on supersaturation.[5,17] In all nucleation events, two important energetic parameters influence rates. The first is the excess free energy associated with the newly formed phase. This is an ensemble property that creates a thermodynamic barrier Δg_c due to the collective behavior of the ions in the solid and liquid phases. The second is an effective kinetic barrier E_A arising from individual reactions such as desolvation of solute ions, attachment to the forming nucleus, and structural rearrangements. Both barriers appear exponentially in the expression for the rate of nucleation J through:[5]

$$J = Ae^{-E_A/\mathbf{k}T}e^{-\Delta g_c/\mathbf{k}T} \quad (1)$$

where A is a pre-factor that is determined by geometric factors and material parameters and Δg_c is a function of the chemical potential $\Delta\mu = \sigma/\mathbf{k}T$, where σ is the supersaturation, **k** is Boltzmann's constant and T is the temperature.

While the exponential dependence of J on σ through the free energy barrier is a universal hallmark of nucleation that, in essence, distinguishes it from a simple chemical reaction, the exact form of A and Δg_c are model dependent. The source of Δg_c is an excess free energy Δg_{ex} of the solid phase above that given by the simple expression $\Delta g = \frac{dg}{dn}\Delta n$ where Δn is the number of molecules passing from the solution to solid phase. Without Δg_{ex} there would be no barrier and precipitation would happen spontaneously at infinitesimal supersaturation *without nucleation*. In classical nucleation theory (CNT), Δg_{ex} arises from the free energy of the interface between the mineral and the surrounding solvent and substrate. When the free energy landscape is flat — that is, the excess free energy is simply determined by the surface area times the interfacial free energy α, which is independent of size — then Δg_c is given by:

$$\Delta g_c = B\frac{\alpha^3}{\sigma^2} \quad (2)$$

where B is a constant that depends on its shape and density (See SI for details). Based on the literature value of 109 mJ/m^2 for the interfacial free energy of calcite in solution,[18,19] the predicted classical barrier to homogeneous nucleation of a calcite rhomb is formidable (Figure 1A and Figure 1E, blue curve), ranging from 175 **k**T to 93 **k**T for $CaCl_2$ and $NaHCO_3$

concentrations between 10 mM and 29 mM — the latter marking the literature value for the solubility limit of ACC.[20] (Note that, at 300K, $1\mathbf{k}T = 2.6$kJ/mol = 0.62kcal/mol.)

As Eqn. 1 shows, the thermodynamic barrier depends upon the cube of the interfacial energy. Consequently, heterogeneous nucleation on surfaces that reduce the interfacial energy can proceed at dramatically altered rates. In this case, α becomes an effective interfacial energy α_{het} that depends on the interfacial energies of the crystal-fluid, fluid-substrate, and crystal-substrate interfaces through:

$$\alpha_{het} = \alpha_{cf} - h(\alpha_{fs} - \alpha_{cs}) \tag{3}$$

where h is a factor that depends on the aspect ratio of the nucleus (See SI for details). As long as $\alpha_{cs} < \alpha_{fs}$, the value of α_{het} will be reduced from that for the homogeneous nucleus. However, even if the effective α_{fs} equals α_{cs}, that is, the interfacial energies for the crystal-substrate and fluid-substrate interfaces are equal, the barrier will already be reduced by a factor of 1.6 (Figure 1E, red curve) simply because a surface that would have been generated during homogeneous nucleation is now an crystal-substrate interface that carries no energy penalty. A further reduction in α by only 20% to 50% due to $\alpha_{cs} < \alpha_{fs}$ would lead to a decrease in the barrier by a factor of 3 to 13 (Figure 1E, green and orange curves). Given that nucleation rate depends exponentially on this barrier, these large reductions mean that surfaces have the potential to completely alter the dynamics and pathways of calcite formation.

In truth, the free energy landscape is unlikely to be flat at small sizes. Δg_{ex} must approach zero at the size of a molecule and probably exhibits local minima and maxima at very small cluster size as certain configurations expose more or less favorable coordination geometries for the surface ions (Figure 1D). While these variations in Δg_{ex} are easy to account for by expressing α as a function of size, they do little to change the basic physics of the nucleation process. Nonetheless, they can potentially have significant effects on the magnitude of the barrier if the size at which that barrier is reached — i.e. the critical size — becomes comparable to the dimensions at which size effects begin to emerge (Figure 1B), or where local (or global) minima in the free energy landscape create a population of metastable (or stable) clusters that can

aggregate to form a critical nucleus (Figure 1C). (For an analysis of how these features impact Eqns. 1 and 2, see the SI.)

Unfortunately, not much is known about the size dependence of α. What little data do exist suggest a slight rise with decreasing size, followed by the beginning of a decrease in magnitude,[21] but those data do little to constrain the dependence in the region below 5nm diameter, which is greater than the 1-3 nm critical size seen in Figure 1A. Theoretical treatments suggest that even a single formula unit already possesses much of the energetic features of the bulk.[22] This suggests the fall-off in interfacial energy may not occur until diameters below 1 nm, though these simulations were performed for molecular solids and can not be directly translated to ionic crystals like calcite. However, metadynamics simulations of equilibrium calcite structure suggest the energetic features of the bulk are still manifest below 2 nm.[23] Indirect evidence for a complex dependence on size comes from both cryoTEM[11] and ultra-centrifugation data[8] that suggest there is indeed a population of sub-critical clusters (commonly referred to as pre-nucleation clusters) with a tight size distribution, which implies there is a minimum in the free energy vs. size. In fact, titration-based studies on the amount of calcium inferred to be bound in these clusters concluded that they occupy a global minimum, i.e., the free energy of the pre-nucleation clusters lies *below* that of the free ions.[8]

Deviations from a flat landscape will change the dependence of Δg_c on σ (Eqn. 2). In the case of a size dependent α, the change can be complex and depends on the form of the size dependence. For nucleation by aggregation of clusters that occupy a local minimum in the free energy, the dependence becomes:

$$\Delta g_c = B\frac{\alpha^3}{(\sigma^2 \pm C)} \tag{4}$$

where C is a constant that depends on the shape factor, the cluster radius and the excess free energy of the cluster, and the plus or minus sign depends on whether the minimum in Δg is local or global (See SI for details). If it is a local minimum (Figure 1D, solid green line), then the clusters are metastable, they carry excess free energy above the free ions, the plus sign applies and the barrier is reduced. If it is a global minimum (Figure 1D, dashed green line), then the clusters lie below the free ions, the minus sign applies and nucleation by cluster aggregation

brings with it an extra energy cost (See SI for details). This is the case for pre-nucleation clusters, which were found to lie about 18kJ/mol below the free ions.[24] Thus creation of a super-critical nucleus by aggregation of pre-nucleation clusters would bring with it a larger barrier than aggregation of free ions, regardless of whether the end product is an amorphous or crystalline phase.

In the case of calcite nucleation by metastable clusters, for cluster radii below 2 nm and a reasonable range of excess free energies — such as those used in Figure 1C, the magnitude of C in Eqn. 4 is less than 10% of σ over the range used in this study. The small magnitude of C relative to σ has two consequences for the current study. First, measurements of the dependence of calcite nucleation rate on supersaturation will not distinguish between ion-by-ion and cluster-by-cluster addition; the classical expressions will hold in either case. Second, because the effect of clusters is likely to be too small to detect, if the classical dependence is not observed, then size dependence of α is the likely source of the deviation.

3. Calcite nucleation rates on carboxyl-terminated SAMs

SAMs of 16-mercaptohexadecanoic acid (MHA) and 11-mercaptoundecanoic acid (MUA), both of which are carboxyl-terminated but differ in the length and parity of the carbon chain, were prepared on Au (111) substrates using previously described methods (See SI for details).[12] The SAMs were suspended upside down in a custom-built flow cell in the focal plane of an inverted optical microscope (See SI and Figure S1 for details). A mixture of $CaCl_2$ and $NaHCO_3$ solutions with equal final concentrations of between 20 and 35 mM were flowed through the cell at constant rates under conditions that ensured nucleation was controlled by the reaction kinetics at the SAM surface rather than by diffusion or mixing. (See SI for details.)

For each concentration, the number of crystals in a fixed area was determined as a function of time (Figure 2A-D). Plots of the number of nuclei vs. time (Figure 2E) produced S-shaped curves exhibiting a linear rise and an approach to saturation marking the time when the density of nuclei became too great for subsequent events to be independent. The slope of the linear region gave the steady-state nucleation rate J (number of nuclei per unit area per unit time). (σ is defined as $ln\left(\frac{\{Ca^{2+}\}\{CO_3^{2-}\}}{K_{sp}}\right)$ where K_{sp} is the solubility product and $\{Ca^{2+}\}$ and $\{CO_3^{2-}\}$ are the

Ca^{2+} and CO_3^{2-} activities, respectively.)

While qualitatively similar behavior was observed for both the MHA (C-16) and MUA (C-11) films, we found the nucleation rate was greater on MHA over the entire supersaturation range explored here. In addition, in accord with previous reports, nucleation occurred on distinct crystallographic planes for the two different SAMs.[15] The even parity MHA SAM induced nucleation almost exclusively on the (012) plane (Figure 3A), while on the odd parity MUA SAM nucleation occurred primarily on the (013) face (Figure 3B), though 30-40% of the crystals exhibited orientations between (012) and (015), and also included sporadic (104) and (001) orientations (Figure 3B insets). In contrast, under identical conditions, nuclei on SAM-free gold films were few in number and exhibited random orientations (Figure 3C).

Analysis of nucleation data such as those given in Figure 2E shows that J exhibits the dependence on σ expected from CNT through Eqns. 1 and 2 (Figure 2F). From the slope of $ln(J)$ vs. σ^{-2} we obtain values for α of 72 mJ/m^2 for MHA and 81 mJ/m^2 for MUA, both of which are substantially smaller than the value of 109 mJ/m^2 for calcite in bulk solution[18,19]. These differences in interfacial energy have a dramatic impact on nucleation rates. For example, in the middle of the supersaturation range explored here, the corresponding free energy barriers for nucleation on MHA, MUA and in bulk solution are found to be 19$\mathbf{k}T$, 27$\mathbf{k}T$ and 105$\mathbf{k}T$, respectively. All other factors being equal, these differences alone would correspond to relative nucleation rates $J_{MHA} : J_{MUA} : J_{sol}$ of $1 : 3.4\text{x}10^{-4} : 4.5\text{x}10^{-38}$, although the advantage of the MHA film over that of the MUA film is somewhat reduced because it also produces a larger value of E_A by about 7±3$\mathbf{k}T$ (as can be seen from the smaller value of the y-intercept for MHA when extrapolated to $\sigma^{-2} = 0$). These results show that calcite nucleation on these canonical SAMs proceeds as expected from CNT and that both the enhancement of nucleation on the SAMs relative to bulk solution and the advantage of the SAM with even parity over that with odd parity can be explained in purely classical terms through differences in interfacial energy.

4. Simulations of SAM structure and interfacial energy

To understand the source of these differences we performed molecular dynamics (MD) simulations on odd (C-15) and even (C-16) parity carboxylated SAMs using previously

developed methods (See SI for details) and examined the differences in SAM structure, the resulting calcite orientations, and the interfacial energies. The radial distribution functions (RDFs) for the C-C atoms within the monomer chains are, as expected, identical for both SAMs (Figure 4a). However, while the first peak (i.e. the nearest neighbor separation) for the headgroup-carbon-to-headgroup-carbon is also identical, there is an extra peak at ~6.5 Å in the odd SAM that is absent in the even SAM (Figure 4b). Also, the RDF for the headgroup-C-to-O (not shown) shows the same peaks for both the even and odd SAMs but the second peak at ~ 5.8 Å is larger for the odd SAM.

These structural differences can be observed through visualization of the SAMs, which shows that the headgroups of the even SAM maintain six nearest neighbors throughout the simulations (Figure 4C), while those of the odd SAM occasionally produce five nearest neighbors with the sixth headgroup pushed to a further separation (Figure 4D). This effect originates from the O-O interactions between the headgroups. In the even SAM, the vector pointing from one oxygen to the other oxygen within a single headgroup (the O-O vector) exhibits an even distribution about 0°, i.e., its average is parallel to the substrate surface (Figure S2). In the odd SAM, however, the angular distribution of the O-O vector is more complex and has an average that is non-zero, peaking at about 22°, demonstrating a that there is a preference for one O to be pointing out of the SAM more than the other (Figure S2). Thus the oxygens of the odd SAM can find themselves pointing directly at each other and thereby generating an energetically unfavorable Coulombic repulsion. This, in turn, causes headgroups to be pushed out of the nearest neighbor shell and leads to the 5+1 arrangement seen in the RDF.

Simulations of calcite nucleation on these SAMs reflect these differences in SAM order. Because simulating nucleation directly from ions in solution is not feasible with current computing resources, even using techniques like metadynamics, anhydrous ACC in contact with the SAMs was used as the starting point. These simulations modeled the formation and growth of the critical nucleus, which would be expected to be anhydrous in the experiments. Therefore the main difference between the simulations and the experiments is the arrival process of the ions, which should not influence the equilibrium structure and energetics of the interface with the SAM. The simulations identify the most energetically accessible crystal-SAM interface and are therefore complementary to the experiment.

Analyzing the results of previous crystallization simulations[25] that used an identical simulation setup to our own, we find for the even parity SAM, crystals are predicted to nucleate on the (012) plane in accordance with the experiments. However, on the odd parity SAM the plane of nucleation is defined by a mix of polar calcite faces such as (001) and (01x) and no single crystal plane of nucleation is formed, once again giving reasonable agreement with experiment. Here the inability to select a single orientation is due to the structural disorder in this film. The predicted interfacial energies are also in reasonable agreement with the experiments, giving 56 and 102 ± 6 mJ/m^2 for the even and odd SAMs, respectively. The trends observed here are expected to be maintained over a wide range of monomer carbon chain lengths, though the exact values of the energies will differ due to the increased or decreased effect of the substrate for shorter and longer monomers, respectively.

5. Nucleation pathways

These findings support the conclusion that the classical viewpoint of nucleation control through minimization of crystal-SAM interfacial energy can describe nucleation in this system and appear to be in conflict with the proposed model for calcite formation as a non-classical process.[8,11,12,24,26] In particular, they raise the question of how our results can be reconciled with those of previous studies that concluded: 1) nucleation of calcite occurs via an ACC precursor and 2) $CaCO_3$ solutions contain pre-nucleation clusters that aggregate to form this precursor. To address these apparent discrepancies we investigated the pathway of calcite formation on SAMs using Raman spectroscopy, *in situ* AFM imaging, optical microscopy and TEM analysis.

Raman spectroscopy provides an unambiguous means for identifying the phase of calcium carbonate precipitates. Raman spectra collected on samples that were quenched during the nucleation rate experiments by switching the incoming fluid from $CaCO_3$ solution to ethanol corresponded to that of calcite regardless of particle size investigated (Figure 5). However, sub-100 nm particles seen in SEM images (Figure S3) were below the threshold for obtaining useful spectra. To assess these particles, we reproduced the conditions of the optical experiments using an AFM in place of the optical microscope (See SI for details). When these experiments were performed using MHA SAMs as substrates, all particles that appeared remained intact and grew in size. Even at the earliest stage of formation captured by the AFM, these particles possessed

the typical rhombohedral shape of calcite and exhibited the orientation seen at larger size that results from nucleation on an (012) face (Figure 6A-D).

When the same experiments were performed using an OH terminated SAM (mercapto-undecanol, MUO), at all supersaturations investigated — including concentrations that were highly undersaturated with respect to ACC based on the accepted bulk solubility — within the first minute of imaging we observed the formation of roughly spherical nanoparticles characteristic of ACC whose number and size were dependent on the solution concentration (Figure 6E). Unlike the result with MHA SAMs, these particles did not continue to grow in size. Instead, after a short period of time they began to dissolve (Figure 6E-G) in response to the formation of the more stable calcite phase elsewhere in the cell. In parallel experiments using identical solution mixtures, these nanoparticles were collected on filters and examined by high resolution TEM, which revealed them to indeed be amorphous (Figure 6H).

Despite *in situ* AFM observations on many tens of these ACC particles, in no instance did we observe their direct transformation into calcite. Rather, only dissolution was observed. However, the AFM only samples small areas (< 100x100 μm^2) so we may have simply missed a transformation event that occurred out of the field of view. To circumvent this limitation, we utilized the fact that ACC particle size is dependent on supersaturation, which can be driven to high values by introducing carbonation via gaseous diffusion from an ammonium carbonate source, in order to generate a film of ACC particles with diameters of 100s of nm (See SI and Figure S4 for details). As expected, when we used the OH-terminated MUO on Au we observed the formation of ACC, most of which fell on the SAM from the solution. However, this film of ACC particles rapidly dissolved back into solution as calcite rhombs nucleated and grew at their expense (Figure 7A-C, Movie S1).

We note that in no instance could we definitively conclude that a calcite rhomb formed through direct transformation of a pre-existing ACC particle. In a number of cases, the rhomb formed from a distinct particle that deposited on the MUO surface and immediately began to grow. The fact that ACC formation occurred before any calcite surface nucleation events took place explains why rates of calcite nucleation on these films showed no dependence on the initial solution supersaturation (Inset, Figure 2F). Once ACC formed homogenously, the solute

concentration immediately became fixed at the solubility of ACC. Thus, in essence, all calcite nucleation occurred at the same supersaturation, regardless of the initial solution conditions.

When the carbonate diffusion experiments were performed using the MHA SAMs, the progression of events was completely reversed from that seen on MUO (Figure 7D-F, Movie S2). The first particles to appear formed directly on the SAM surface and grew into calcite rhombs. None of these particles ever underwent dissolution. Well after they could be clearly identified as rhombs, ACC began to form in solution and deposit on the surrounding Si substrate. Some of this ACC also deposited on the SAM, but dissolved immediately due to presence of the growing calcite crystals. As the Ca^{2+} level in the surrounding solution decreased, even the ACC outside of the SAM began to dissolve due to the continued growth of the calcite rhombs. When SAMs were used that extended across the entire substrate, no ACC was observed, because the formation of calcite across the full extent of the film prevented the supersaturation from reaching the required level for ACC formation.

6. Discussion

The results presented above imply that ACC nanoparticles did not serve as direct precursors to calcite in our experiments with carboxyl SAMs. Rather calcite formation resulted from distinct nucleation events. While this result would seem to contradict the previous claims that ACC serves as a precursor to calcite, we note that nearly all previous studies in which this two-step pathway was proposed were carried out at supersaturations well in excess of the solubility limit of ACC[8,11,12] and, with one exception,[11] the transformation of an amorphous particle into a crystal was not directly observed, rather it was inferred from the sequence of events, i.e., ACC formed first and was eventually replaced by one of the crystalline phases. In the case of experiments that utilized carbonate diffusion into a $CaCl_2$ solution,[8] as well as those based on titration of a carbonate buffer,[12] the supersaturation increased continually to the point of nucleation. Thus the large barrier to homogeneous nucleation, which is still in excess of 90kT at the literature value of ACC solubility, may simply have prevented calcite nucleation before conditions that favored ACC formation were reached. Whether the eventual conversion to a crystalline phase occurred by direct transformation from ACC or through dissolution and re-precipitation on crystal nuclei that formed independently is simply not known.

In the cryoTEM study of Pouget et al.,[11] direct conversion was inferred from *ex situ* images that revealed vaterite nanoparticles within or on larger amorphous particles in contact with a Langmuir monolayer. However, the interfacial energy between the Langmuir monolayer and calcium carbonate crystalline phases is unknown may simply be too high to induce their formation on the timescale of either ACC formation or its conversion to vaterite under the conditions of the experiments. Moreover, because the images are collected ex situ, whether or not they truly capture s solid-state conversion or nucleation of vaterite from solution on the surface of an ACC particle is unknown. Finally, even though the calcite crystals in our study appear to nucleate before ACC forms in the case of MHA and perhaps even separately from the initial ACC nanoparticles in the case of MUO, we cannot rule out the possibility that the calcite nuclei are themselves constructed from pre-critical clusters in solution. As pointed out in section **2**, for a reasonable range of cluster excess free energies, their effect would be undetectable in measurements of J vs. σ. Thus their dynamics would only be reflected in the prefactors A and E_A. As long as the super-critical nucleus that emerges is that of calcite, the rate data will reflect the calcite-SAM interface through the classical expressions. Consequently, there is no obvious contradiction between these studies.

With respect to the pre-nucleation clusters[24], there are two possible scenarios that are consistent with all of the observations. First, the clusters are like any other solution species; they behave as simple ionic complexes, constantly forming unstable sub-critical nuclei that spontaneously fluctuate in size until, by chance, they exceed the critical nucleus size either by ion addition or cluster aggregation. Second, they play no role in nucleation at the relatively low concentrations of these experiments; nucleation is ion-by-ion because the number and diffusivity of the free ions are much greater than those of the clusters or because the kinetic barriers to building an ordered nucleus from ions are much less than those to desolvating and ordering the clusters. A firm conclusion will have to wait until experimental tools enable direct characterization of pre-nucleation clusters in low concentration solutions at surfaces.

Acknowledgements

This research was supported by the U.S. Department of Energy, Office of Basic Energy Sciences, Division of Chemical, Biological and Geological Sciences through Lawrence Berkeley National

Laboratory and as part of the Center for Nanoscale Control of Geologic CO_2, an Energy Frontier Research Center under contract No. DE-AC02-05CH11231. Measurements were performed at the Molecular Foundry, Lawrence Berkeley National Laboratory with support from the Office of Science, Office of Basic Energy Sciences of the U.S. Department of Energy under Contract no. DE-AC02-05CH1123. This research was made with Government support under and awarded by DoD, Air Force Office of Scientific Research, National Defense Science and Engineering Graduate (NDSEG) Fellowship, 32 CFR 168a. CLF and JHH would like to thank funding from UK EPSRC grant number EP/I001514/1; this UK programme grant funds the Materials Interface with Biology consortium. Portions of this work were performed under the auspices of the U.S. Department of Energy by Lawrence Livermore National Laboratory under Contract DE-AC52-07NA27344. The research was also supported by awards to PMD from the US Dept. of Energy (DOE BES-FG02-00ER15112) and the National Science Foundation (NSF OCE-1061763).

References

1. Addadi, L., Joester, D., Nudelman, F., and Weiner, S. *Chemistry-a European Journal*, 2006, **12**, p. 981-987.
2. Braissant O., Gailleau G., Dupraz C., and Verrecchia E.P., *Journal of Sedimentary Research*, 2003, **73**, 485-490.
3. Weiner S., Traub W., Wagner H.D., *J. Struct. Biology*, 1999, **126**, 241-255.
4. Nudelman, F. *et al.*, *Nat. Mater.*, 2010, **9**, 1004-1009.
5. De Yoreo, J.J. and P.G. Vekilov, *Reviews in Mineralogy and Geochemistry*, 2003, **54**, 57-93.
6. Jager, I., and Fratzl, P., *Biophys. J.*, 2000, **79**, 1734-1746.
7. Fang,P-A., Conway, J.F, Margolis, H.C., Simmer, J.P., and Beniash, E., *Proc. Nat'l. Acad. Sc*i., 2011, **108**, 14097–14102.
8. Gebauer D, Volkel A, Colfen H, *Science*, 2008, **322**, 1819-1822.
9. Politi, Y., et al., *Science*, 2004, **306,** 1161-1164.
10. Mahamid J, Sharir A, Addadi L, Weiner S, *Proc Natl Acad Sci USA,* 2008, **105**, 12748–12753.
11. Pouget, E. M. *et al.*, *Science,* 2009, **323**, 1455-1458.
12. Lee, J.R.I., et al., *J. Am. Chem. Soc.*, 2007. **129**, 10370-10381.
13. Aizenberg, J., A.J. Black, and G.M. Whitesides, *Nature*, 1999, **398**, 495-498.
14. Travaille, A.M., A. M., Donners, J. J. J. M., Gerritsen, J. W., Sommerdijk, N. A. J. M., Nolte, R. J. M., van Kempen, H., *Adv. Mater.*, 2002 **14**, 492-495.
15. Han, Y.-J. and J. Aizenberg, *Angew. Chem. Int. Ed.,* 2003, **42**, 3668-3670.
16. Freeman C.L., Harding J.H., and Duffy D.M., *Langmuir,* 2008, **24**, 9607-9615.
17. Wallace, A.F., J.J. DeYoreo, and P.M. Dove, *J. Am. Chem. Soc.*, 2009, **131,** 5244–5250.
18. O. Sohnel and J. W. Mullin, *J. Cryst. Growth*, 1978, **44**, 377-382.
19. O. Sohnel, *J. Cryst. Growth*, 1982, **57**, 101-108.
20. Brecevic, L. and A.E. Nielsen, *J. Cryst. Growth*, 1989, **98**, 504-510.
21. Zhang, H., Chen, B. & Banfield, J. F., *Phys. Chem. Chem. Phys*., 2009, **11**, 2553-2558.

22. G. V. Gibbs, T. D. Crawford, A. F. Wallace, D. F. Cox, R. M. Parrish, E. G. Hohenstein, and C. D. Sherril, *J. Phys. Chem. A*, 2011, **115**, 12933–12940.
23. Harding, J., *J. Chem. Phys.*, 2011 **134**, 044703.
24. Gebauer, D. and Coelfen, H., *NanoToday,* 2011, **6**, 564-584.
25. Quigley, D., et al., *J. Chem. Phys.*, 2009, **131**, 094703.
26. A. Navrotsky, P*roc. Nat. Acad. Sci. U.S.A.*, 2004, **101**, 12096-12101.

Figure Captions

Figure 1 – (A) Dependence of free energy Δg on the length of a side for homogeneous nucleation of an equilateral rhombohedron of calcite for $CaCl_2$ = $NaHCO_3$ concentrations (supersaturations) of: Blue – 10mM (σ = 3.5); Red - 15mM (σ = 4.0); Green – 23mM (σ = 4.5); Orange – 28mM (σ = 4.8). (B) Effect of size dependent excess free energy on Δg_c where $\alpha = \alpha_\infty\{1\text{-}\exp[-(L\text{-}L_0)/L_\infty]\}$ and α_∞ is the bulk interfacial energy. Solid curves - 10mM (σ = 3.5) and dotted curves 28mM (σ = 4.8). Values of L_∞, L_0 in nm are: Blue – 0, 0; Red - 0.1, 1; Green – 0.2, 2. (C) Effect on Δg_c of aggregation by clusters of size L = 0.5 nm occupying a local minimum in excess free energy. Solid curves - 10mM (σ = 3.5) and dotted curves 28mM (σ = 4.8). Ratio of excess free energy to bulk surface energy is: Blue - 1/40; Red - 1/10; Green - 1/2. Note that values of Δg_c make no sense below L=0.5 nm, because clusters of this size are assembled to make the critical nucleus. (D) Dependence of excess free energy (Δg_{ex}) on particle size. Blue line – flat energy landscape; Red line – simple size dependence; Green line – Size dependence with local minima and maxima; Green dashed line – global minimum defining stable population of clusters with narrow size distribution. (E) Dependence of free energy barrier Δg_c on σ for homogeneous nucleation of a calcite rhomb with α = 109 mJ/m^2 (blue line) and heterogeneous nucleation of a calcite rhomb on an (012) face with α_{het}/α_{cf} of: Red - 1.0; Green - 0.8 and Orange - 0.5.

Figure 2 – Rate of calcite nucleation on MHA and MUA SAMs. (A-D) Sequential optical images collected at t =100, 300, 350 and 450 s. Each image is: 0.49mm x 0.49mm. (E) Typical dependence of number of nuclei vs. time. (F) Dependence of ln(J) on σ^{-2} showing that MHA films produce shallower slope and lower intercept than MUA films. Inset - Same as in F, but for nucleation on the OH-terminated mercapto-undecanol (MUO) SAM in solutions produced by mixing solutions of $CaCl_2$ and Na_2HCO_3 at a pH of 10.55.

Figure 3 – SEM images showing number density and orientation of calcite crystals on (A) MHA, (B) MUA, and (C) bare gold surfaces. Scale bars are: main images - 100 μm; insets - 10 μm.

Figure 4 – (A, B) Radial distribution functions from MD simulations of odd and even parity

SAMs for (A) the carbon in the chains with the other carbon in the chains and (B) the carbon in the headgroups of the monolayers with the other carbon in the headgroups for the even SAM (dashed magenta) and odd SAM (solid black). (C, D) Snapshot from simulations demonstrating the different arrangement of the headgroups by viewing the monolayer from above the surface for (A) even and (B) odd SAMs. The nearest neighbor C-C separations are indicated with a dotted line while the increased separation between two carbons in the odd SAM is highlighted as a solid line.

Figure 5 - Typical Raman spectra of particles formed right after the incubation time for 30mM solutions. (A) optical microscopy image of of $CaCO_3$ particles collected on gold 75 seconds after mixing the solutions, (B) Raman spectra where color of curve corresponds to that of solid circle in (A).

Figure 6 – (A-D) Series of sequential *in situ* AFM images showing nucleation on MHA SAM under flowing 25mM solution with pH 8.4. First particles to appear have typical morphology seen for rhombohedral calcite nucleating on (012) face and grow in number and size with time. Time between frames is 93.2 s and scale bars are 1.0 μm. (D-F) Series of sequential *in situ* AFM images showing dissolution of initially formed nanoparticles in flowing 13 mM $CaCO_3$ solution at room temperature and pH 8.4 on the surface of MUO. Times at which these frames were captured are (D) 68 s, (E) 128 s and (F) 190 s, where t=0 corresponds to the moment when the calcium and bicarbonate solutions were mixed. The average height of nanoparticles decreases from (D) 64.2±9.7 nm to (E) 53.2±12 nm and to (F) 33.2±14 nm. Scale bars are 200 nm. (G) TEM image and diffraction pattern (inset) of nanoparticles captured from 25 mM $CaCO_3$ using methodology described in SI and showing particles are amorphous. Scale bar is 100 nm.

Figure 7 – (A-C) Still images from movie S1 showing the pathway of calcite formation during diffusion of carbonate into $CaCl_2$ solution on an MUO SAM. The appearance of ACC is followed by nucleation of calcite and concomitant dissolution of the ACC film. Frame times are 830, 1,892 and 3,742 s. (D-F) Still images from movie S2 showing the pathway of calcite formation during diffusion of carbonate into $CaCl_2$ solution on an MHA SAM. Calcite first appears only on the MHA film. As it grows, ACC then begins to deposit from solution until the Ca^{2+} is sufficiently depleted that ACC dissolves as calcite continues to grow. Frame times are

280, 700 and 1,500 s.

Figure 8 – Schematic showing pathways of calcite formation on (A) carboxyl- and (B) hydroxyl-terminated SAMs. With carboxyl-terminated SAMs, free ions and ion pairs, pre-nucleation clusters or dense liquid droplets aggregate directly on the SAM to form a critical nucleus of calcite, which then grows by addition of these species. ACC then subsequently forms in solution and dissolves as it falls towards the SAM, thereby feeding the growing crystal. With hydroxyl-terminated SAMs, free ions and ion pairs, pre-nucleation clusters or dense liquid droplets first aggregate to form ACC nanoparticles in the solution. The ACC particles then land on the SAM, forming an ACC film. Subsequent nucleation of calcite either directly on the SAM or in the surrounding solution then leads to dissolution of the ACC film as the calcite grows.

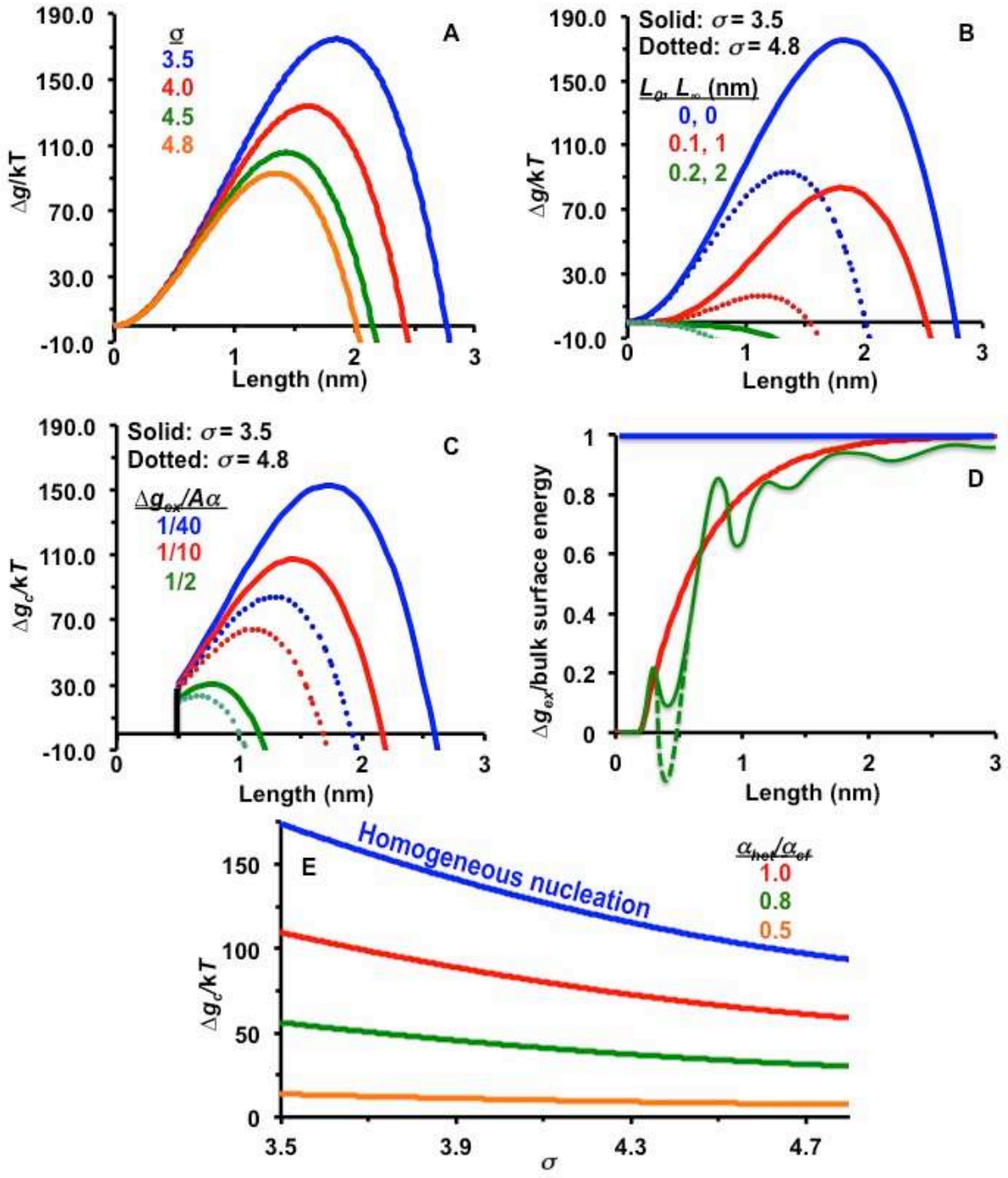
A
σ
3.5
4.0
4.5
4.8
Δg/kT
Length (nm)
B
Solid: σ = 3.5
Dotted: σ = 4.8
L_σ, L_∞ (nm)
0, 0
0.1, 1
0.2, 2
C
Δg_ex/Aα
1/40
1/10
1/2
Δg_c/kT
D
Δg_ex/bulk surface energy
E
Homogeneous nucleation
α_het/α_ef
1.0
0.8
0.5
σ

Figure 1

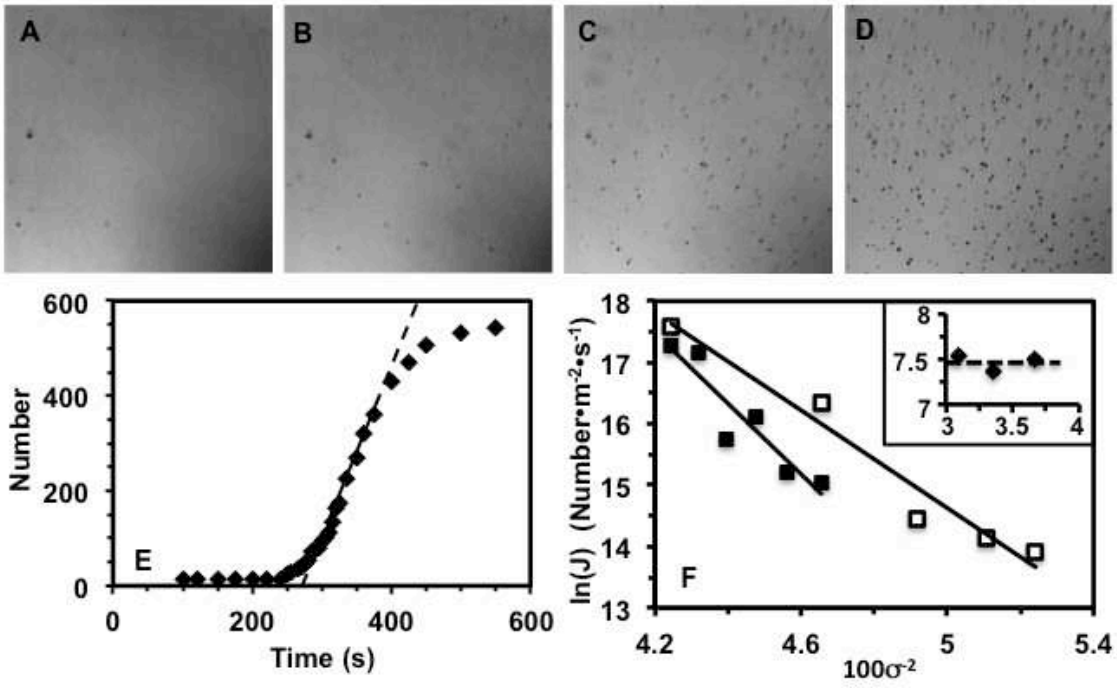
A
B
C
D
600
400
200
0
Number
E
0
200
400
600
Time (s)
18
17
16
15
14
13
ln(J) (Number•m-2•s-1)
F
8
7.5
7
3
3.5
4
4.2
4.6
5
5.4
100σ-2

Figure 2

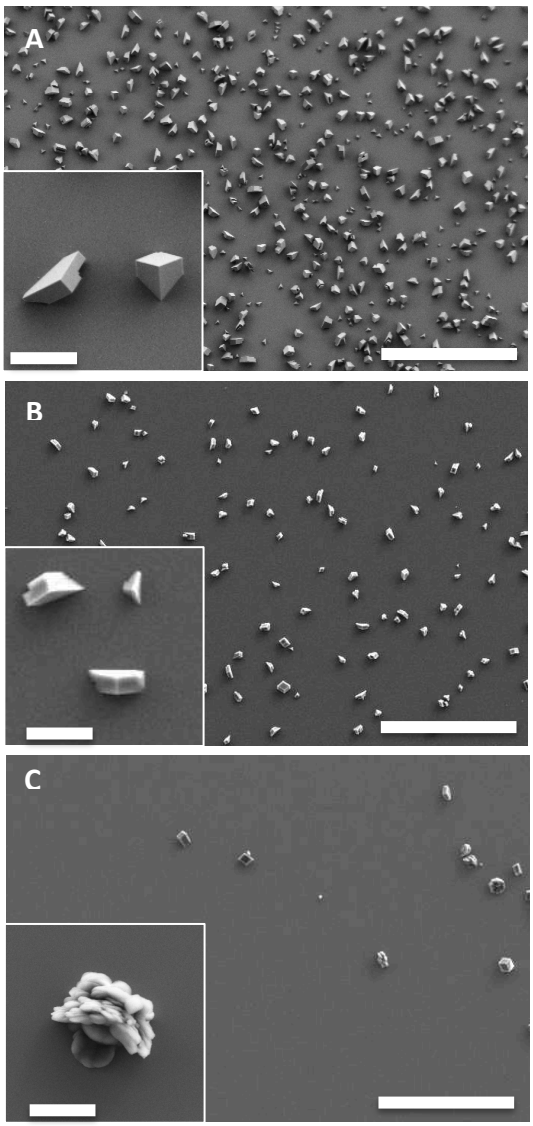

Figure 3

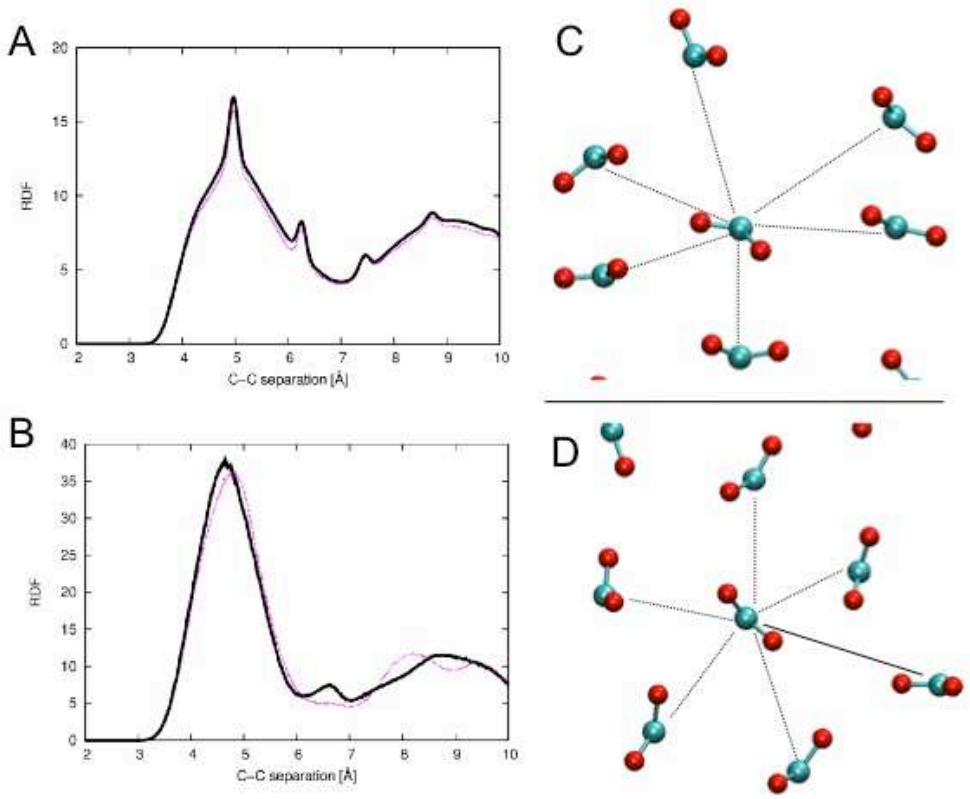

Figure 4

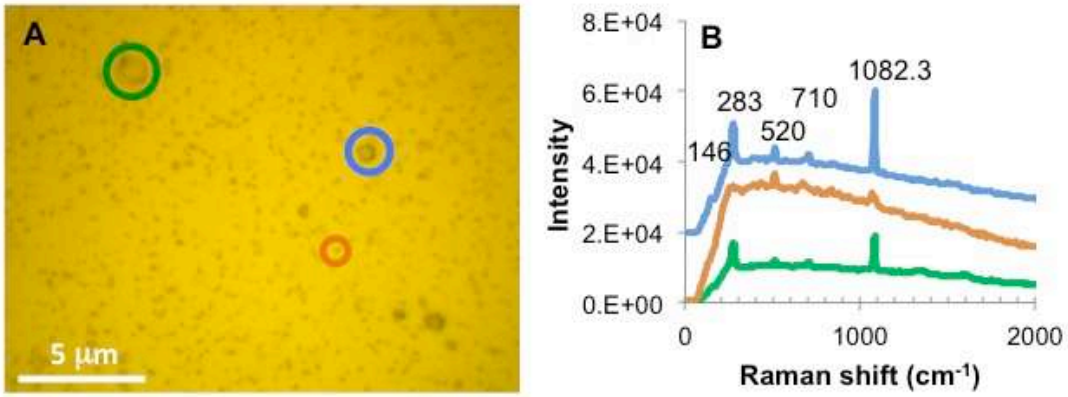
A
5 µm
B
8.E+04
6.E+04
4.E+04
2.E+04
0.E+00
Intensity
146
283
520
710
1082.3
0
1000
2000
Raman shift (cm-1)

Figure 5

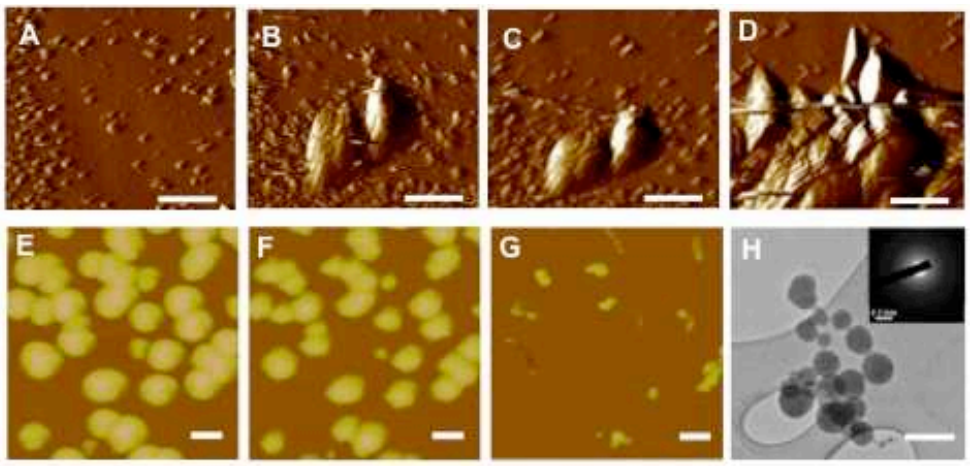

Figure 6

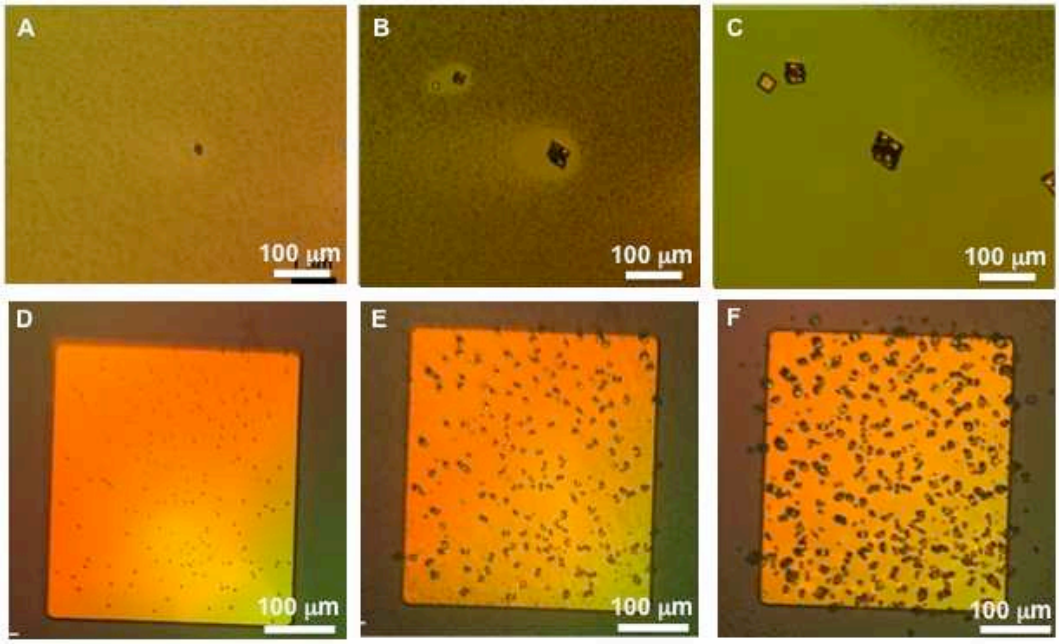

Figure 7

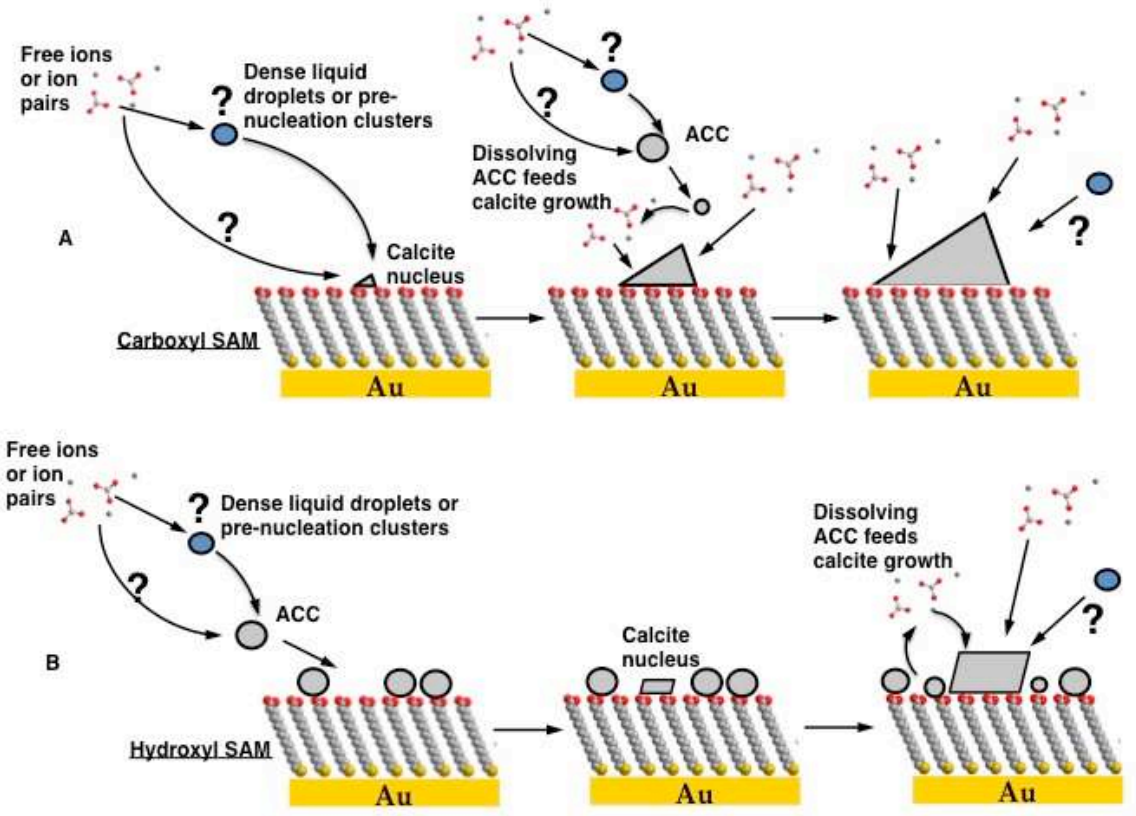
Free ions or ion pairs
Dense liquid droplets or pre-nucleation clusters
ACC
Dissolving ACC feeds calcite growth
A
Calcite nucleus
Carboxyl SAM
Au
Au
Au
Free ions or ion pairs
Dense liquid droplets or pre-nucleation clusters
ACC
B
Calcite nucleus
Dissolving ACC feeds calcite growth
Hydroxyl SAM
Au
Au
Au

Figure 8

Supplementary Information

Experimental methods

SAM Preparation: The MHA and MUA monolayers on gold surfaces were carried out by immersing gold substrates for 24 to 30 hours into 2 mM MHA or MUA solutions of 95% ethanol and 5% acetic acid.[1] After removal from the ethanolic solutions, the gold substrates were thoroughly rinsed with the corresponding pure solvent, 5% acetic acid in ethanol, and then dried by flow of nitrogen gas. SAMs were covered by DI water to eliminate potential oxidization and then instantly placed in the flow cell of the optical microscope.

Solution preparation: Ca^{2+} and CO_3^{2-} solutions were prepared from DI water and reagent grade $CaCl_2$ and $NaHCO_3$ for concentrations of: 10 mM, 18 mM, 20 mM, 21 mM, 22.5 mM, 24 mM, 25 mM, 26 mM, 27 mM, 28 mM, 29 mM, and 30 mM. Outside of this concentration range, we found that nucleation rates were either too fast or too slow to be successfully analyzed. The activities of Ca^{2+} and CO_3^{2-}, and supersaturation relative to calcite and ACC were calculated using MINTEQ[2] (Table S1). The equilibrium solubility products (Ksp) of calcite and ACC were based on the values of $10^{-8.48}$ and $10^{-6.393}$.[2,3]

Table S1

	$\{Ca^{2+}\}$	$\{CO_3^{2-}\}$	σ (calcite)	σ (ACC)
10 mM	4.45E-03	2.48E-05	3.506	-1.299
15 mM	5.84E-03	3.14E-05	4.014	-0.791
20 mM	7.04E-03	3.71E-05	4.368	-0.437
21 mM	7.26E-03	3.81E-05	4.425	-0.379
22 mM	7.48E-03	3.92E-05	4.483	-0.322
23 mM	7.69E-03	4.02E-05	4.536	-0.269
24 mM	7.90E-03	4.11E-05	4.58	-0.218
25 mM	8.11E-03	4.21E-05	4.635	-0.170
26 mM	8.31E-03	4.30E-05	4.683	-0.122
27 mM	8.51E-03	4.40E-05	4.727	-0.078
28mM	8.71E-03	4.49E-05	4.770	-0.034
29 mM	8.90E-03	4.58E-05	4.812	0.0069
30 mM	9.10E-03	4.67E-05	4.853	0.0483

Optical microscopy: A schematic image of the optical setup is illustrated in Figure S1. $CaCl_2$ and $NaHCO_3$ solutions were loaded into separate syringes of an automated syringe pump. $CaCl_2$ was first injected into the fluid cell before flowing through an equal mixture of $CaCl_2$ and $NaHCO_3$ solutions of equal concentrations in order to achieve better face-selective control.[4] We tested flow rates from 0.5 to 5 mL/min and found that the $CaCO_3$ nucleation rate increased as the flow rate increased from 0.5 to 2 mL/min, but did not change if the rate was increased further. Therefore, the flow rate was set to 2 mL/min, to yield nucleation rates independent of flow rate. This ensured that the nucleation was not limited by diffusion but was controlled by the nucleation reaction at the SAM surface. The tubing length was adjusted to ensure adequate mixing with little or no nucleation occurring prior to entering the fluid cell A tubing length of around 38 cm provided the highest rate of nucleation on the SAMs. The SAMs were placed upside down in the flow cell to prevent spurious nuclei from the solution from landing on the SAMs. $CaCO_3$ nucleation on the SAMs was imaged *in situ* using an inverted optical microscope in an area of $0.65 \cdot 0.49$ mm^2. Because the critical radius of a $CaCO_3$ nucleus was expected to be well below the resolution limit of the optical system, the nuclei were too small to be observed by the optical microscope at the instant of formation, so we assumed that each observed crystal developed from one nucleus. This assumption was reasonable because the observed nucleation density was so low that the average distance between neighboring nuclei was much greater than the size at which the nuclei became visible. The observed linear dependence between number of nuclei and time after the onset of nucleation validates this assumption.

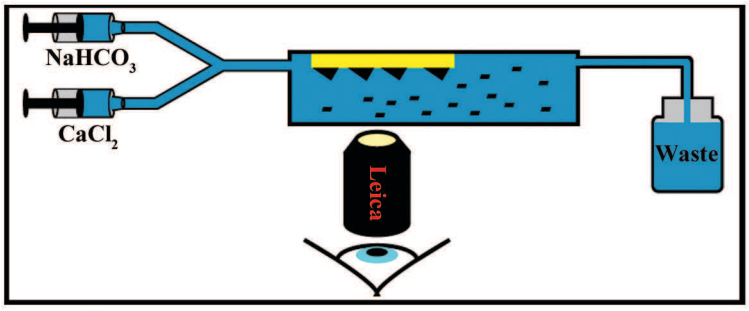

Fig. S1 – Schematic of experimental set-up for measuring nucleation rates. The SAM is suspended upside-down in a flow-through cell and imaged using an inverted optical microscope to measure nucleation rates as supersaturated calcium carbonate solutions are continuously pumped through the cell to maintain constant supersaturation.

Molecular dynamics simulations: Molecular dynamics simulations were performed using the DL_POLY classic code (version 1.4)[5] with a time step of 1 fs. Simulations were all performed using the NVT hoover thermostat with a relaxation time of 0.02 ps at a temperature of 300 K. The configurations of the SAMs were those used in previous simulations[6], with a total of 48 chains arranged in a hexagonal layout in a box measuring 33.2 Angstrom x 28.8 Angstrom in the plane of the monolayer. The SAM chains were 16-mercaptohexadecanoic acid (even) and 15-mercaptopentadecanoic acid (odd). For all the simulations described the SAMs were fully ionised and therefore 24 Ca^{2+} cations were introduced to the system to maintain charge neutrality. A total of 480 water molecules were placed above the SAM surface for simulations of the SAM-water interface. The simulations with $CaCO_3$ used the final geometries from previous metadynamics crystallization simulations[7]. In these simulations the 480 water molecules were placed in contact with the exposed $CaCO_3$ surface not at the interface with the SAM. The sulfur atom at the base of each chain was fixed during the simulation but all other atoms were allowed full mobility. The united atom model from the CHARMM forcefield[8,9] was used to described the SAM chains with the head groups modeled explicitly. Water molecules were modeled with the TIP3P model[10] and the $CaCO_3$ ions were modeled with the Pavese forcefield[11.12]. Cross-term interactions were derived via the method of Schroder et al[13] as demonstrated for $CaCO_3$[14]. Simulations were run until the 250 ps block energies showed a variation of less than 20 kJ/mol (typically 5 ns) from the simulation average and the energies reported were collected over the final 1 ns.

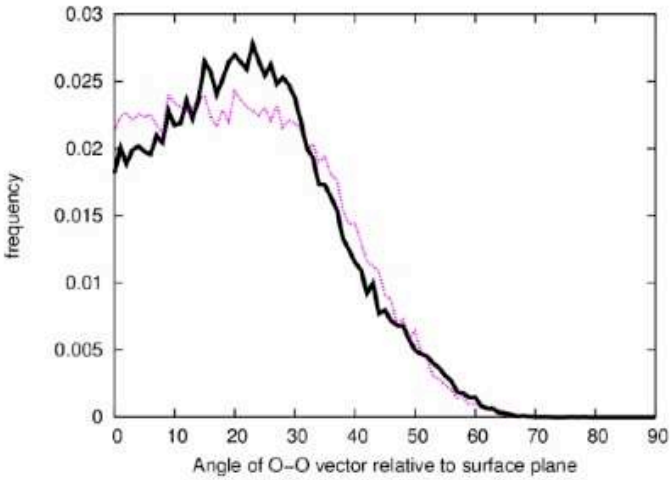

Fig. S2 - Angular distribution of the O-O vector with respect to the surface plane of the SAM for the even (dashed magenta) and odd (solid black) SAMs in contact with water.

It is not possible to directly extract free energies from molecular dynamics simulations as entropy is related directly to the partition function and requires special methods for its calculation. Therefore the energies returned are configurational energies (since the simulation is performed within an NVT ensemble). However, the difference between these values for odd and

even configurations would be expected to be similar to the difference between the experimental free energies since the configurations of the odd and even SAMs are much alike and so the vibrational component of the simulations will be nearly identical in both odd and even SAMs and therefore tend to cancel out. Moreover, since the process of determining the interfacial energies requires finding the differences between two simulations the vibrational contributions should cancel even for the individual values. Absolute crystal-film (acf) and film-solution (afs) interfacial energies cannot be calculated from simulation as there is no suitable reference state for the isolated film. Calculation of the difference between acf and afs (i.e. acf-afs) is possible (since the reference state of the isolated film cancels out) by performing multiple simulations of the film-solution, film-crystal and crystal-solution interfaces and determining the differences between them which can then be used within equation S1 to determine the interfacial energy required. See reference 15 for a detailed discussion of the simulations necessary to calculate this value.

Raman analysis: Samples were quenched in the optical cell by changing the flow from calcium carbonate solution to ethanol, as described previously for quenching of calcium phosphate samples.[16] Precipitates collected right after the exhibited Raman patterns characteristic of calcite with peaks at 154 cm^{-1}, 284 cm^{-1},710 cm^{-1} and 1084 cm^{-1} [17,18]. However, the distinctive broad peak of ACC at 150-300 cm^{-1} [19,20] did not occur in any of the patterns. Since the volumes of the smallest particles are at the lower detection limit of micro-Raman, the peaks are not as sharp as the ones from the other two morphologies. (The 520 cm^{-1} peak is that of Si from silicon wafer.)

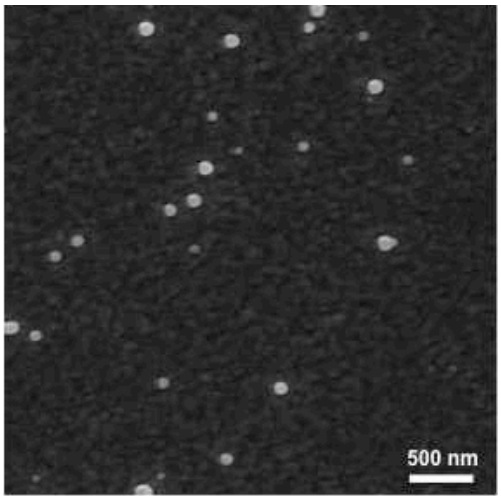

Fig. S3 – SEM image of 23 mM sample on MUA film recovered from optical flow cell showing sporadic occurrence of sub-100 nm particles. Mottled background reflects roughness of sputtered Au films used as substrates for SAMs.

Atomic Force Microscopy: *In-situ* atomic force microscopy was measured by using an AFM liquid cell with either contact or tapping mode AFM (Digital Instruments J scanner, Nanoscope IIIa and V controllers, Veeco Metrology, Inc., Santa Barbara, CA) using hybrid probes consisting of silicon tips on silicon nitride cantilevers (Sharp Nitride Lever, k = 0.35 N/m, tip radius < 10 nm; Bruker AFM

probes, and Hydra, k = 0.035 N/m, tip radius < 10 nm; AppNano.). The tapping mode was adopted in these experiments while applying a loading force less than 50 pN using optimized feedback and set-point parameters for stable imaging conditions. About 100 μL of growth solutions were injected into the sealed liquid cell and the image was captured immediately after the solution injection. Measurements were made by mixing equal $CaCl_2$ and $NaHCO_3$ with the final concentrations of 13 mM and 25 mM on the surface of hydroxyl-terminated SAMs and between 20 mM and 40 mM on the surface of carboxyl-terminated SAMs. SAM preparation followed the same procedure as used in the optical experiments, using MUO and MHA for hydroxyl-and carboxyl-SAMs, respectively. In order to increase the image stability and nuclei density, *in-situ* AFM experiments were also carried out by diffusion method with ammonium carbonate diffusing into 50 mM $CaCl_2$ on the surface of OH terminated SAMs or mica. No obvious differences were observed between these two methods or substrates. The first particle was observed within 1 min for mixing method and up to 30 min for diffusion method, however, all of these particles were dissolved within 5min when the rhombohedral crystal formed separately.

TEM analysis: TEM samples used the same solution preparation method described for the AFM analysis. Subsequent to filtering the solutions, equal amounts were pipetted into a 1 mL centrifuge tube and spun at 6000 rpm in a Galaxy Ministar centrifuge (VWR) for 1-2 minutes, depending on concentration. The supernatant liquid was quickly removed and replaced with 200 proof ethanol and the sample was centrifuged for another minute. This was repeated three times. After the final rinse, ethanol was used to wash any solid off the centrifuge tube walls and suspend the material in solution. A drop of this solution was placed on a TEM grid which was immediately placed into vacuum and pumped into the millitorr range. The TEM grid was then removed from vacuum, secured onto a TEM stage, and inserted into a JEOL 2100F operating at 200kV for analysis.

Carbonate diffusion optical experiments: Carbonate diffusion experiments were conducted by placing OH and COOH SAM substrates in a covered 100 mm diameter petri dish, elevating the substrate to just below the inner surface of the lid. A small droplet of a few to a few tens of microliters of $CaCl_2$ solution, 10-50 mM, was placed on the substrate, and a 20 mm diameter

dish containing less than a gram of $(NH_4)_2CO_3$ was placed nearby the substrate in the larger dish. The lid was then replaced on the larger dish and the dish was moved such that the substrate was in the focal plane of a light microscope and the first image was collected, establishing a zero time point. This time point was five to ten seconds after closing the dish. Sequential images were captured every five to ten seconds following the zero time point.

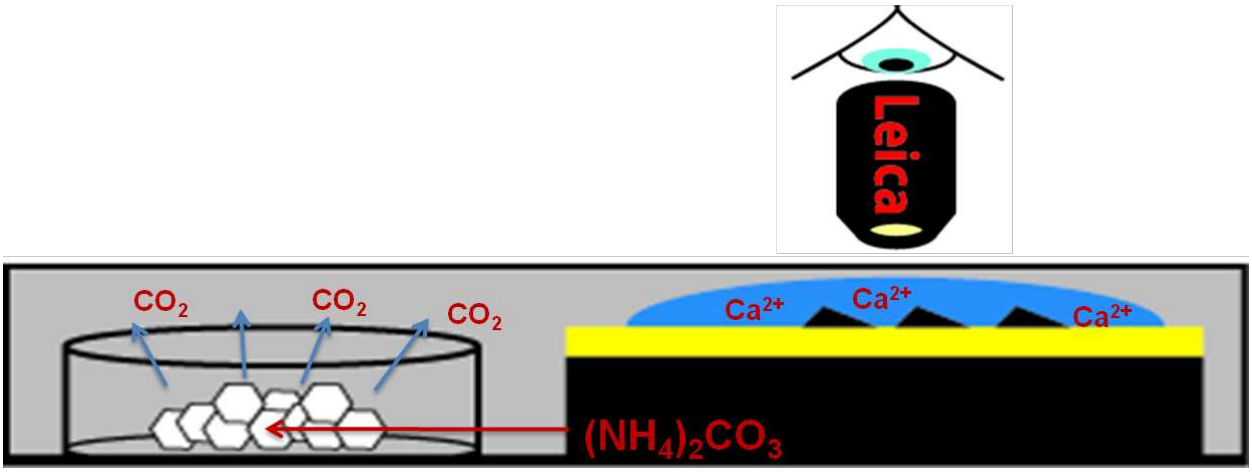

Fig. S4 – Schematic showing set-up for optical experiments to observe calcium carbonate nucleation during diffusion of carbonate into a $CaCl_2$ solution. The upward-facing SAM is covered with a droplet of $CaCL_2$ solution in a closed optically transparent container. $(NH_4)_2CO_3$ is placed in an open dish near the droplet and nucleation is observed through an optical microscope.

Dependence of nucleation rate on supersaturation: In classical nucleation theory (CNT), the free energy change upon nucleation is given by:[5]

$$\Delta g = -\frac{V}{\Omega}\mathbf{k}T\sigma + A_b(\alpha_{cs} - \alpha_{fs}) + A_s\alpha_{cf} \quad \text{(S1)}$$

where V is the volume of the nucleus, Ω is the molecular volume of the growth unit — equal to 6.13E-23 cm^3 for calcite[21] — $\mathbf{k}$ is Boltzmann's constant, T is the absolute temperature, σ is the supersaturation, A_b is the area of the base in contact with the film, A_s is the area of the surface in contact with the solution, and α_{cf}, α_{fs} and α_{cs} are the interfacial energies of the crystal-fluid, fluid-substrate and crystal-substrate interfaces. The thermodynamic barrier is given by the maximum in Δg, which occurs at:

$$\Delta g_c = \frac{f\alpha^3\Omega^2}{(\mathbf{k}T\sigma)^2} \quad \text{with} \quad \alpha = \alpha_{cf} - h(\alpha_{fs} - \alpha_{cs}) \quad \text{(S2)}$$

and the corresponding nucleation rate is given by:

$$J = Ae^{-E_A/kT}e^{-\Delta g_c/kT} \text{ or } \ln(J) = A' - \frac{f\alpha^3\Omega^2}{(\mathbf{k}T)^3}\left(\frac{1}{\sigma^2}\right) \text{ with } A' = ln(Ae^{-\frac{E_A}{kT}}) \quad \text{(S3)}$$

where A is a pre-factor that is independent of σ, and E_A is an effective activation barrier that captures the kinetic barriers to reactions such as desolvation of solute ions, attachment to the forming nucleus and structural rearrangements. Here both f and h are numbers that depend on the aspect ratio of the nucleus. For nucleation on the (012) plane, analysis of the volume and surface areas leads to f = 19.71 and h = 0.525. However, for a large range of nucleation planes, these numbers are nearly identical, varying by no more than about 10%. Because the interfacial energy is raised to the third power in the free energy barrier, these small variations in f have negligible effect (<2.5%) on the values of α extracted from the nucleation rate data.

The interfacial free energy can be generalized to an excess free energy, Δg_{ex}. In this regard, the change in free energy associated with formation of a solute particle is given by:

$$\Delta g = \frac{dg}{dn}\Delta n + \Delta g_{ex} \quad \text{(S4)}$$

In CNT Δg_{ex} is given by the interfacial energy times the surface area of the nucleus, which is assumed to be constant. Consequently, Δg_{ex} scales with the square of the particle size, i.e., $\Delta g_{ex}/A_s = \alpha$ = constant. Two factors that can have a further and significant impact on the nucleation barrier are a more complex size dependence and the existence of local minima in Δg_{ex} vs. size.

The effect of size dependence can easily be incorporated. For example, if the size dependence is given by an exponential rise from a minimum value, then $\Delta g_{ex} = \alpha_\infty A_s\{1\text{-}exp[-(L\text{-}L_0)/L_\infty]\}$. When the critical size is of the order of or less than the dimensions at which the dependence of the excess free energy on size becomes significant, the consequence of is a reduction in the energy penalty associated with creating the critical nucleus. The impact of this effect is shown in Figure 1B.

The effect of clusters can also be incorporated into Eqn S1 by writing:

$$\Delta g = -\frac{V}{\Omega}\mathbf{k}T\sigma + A_b(\alpha_{cs} - \alpha_{fs}) + A_s\alpha_{cf} - \frac{V}{V_{cl}}\Delta g_{ex} \quad \text{(S5)}$$

where V_{cl} and Δg_{Ex} are the volume and excess free energy of a cluster above that of the free ions. For homogeneous nucleation of rhombohedral calcite of side L from spherical clusters of radius r_{cL}, $\frac{V}{V_{Cl}} = \ 0.978 \bullet L^3/4\pi r_{Cl}^3$ giving:

$$\Delta g \ = \ - \frac{0.978L^3}{\Omega}\mathbf{k}T\sigma + 6 \bullet 0.978\mathrm{L}^2\alpha_{cf} - \frac{0.978 \bullet L^3}{\frac{4}{3}\pi r_{cl}^3}\Delta g_{ex} \qquad \text{(S6)}$$

When the clusters lie in a local minimum, Δg_{ex} >0 (Figure 1D, solid green line). Therefore, because the clusters lie higher in free energy than the ions, aggregating them to form a critical nucleus carries less of an energy penalty. On the other hand, if the clusters lie in a global minimum, i.e., they are lower in energy than the free ions, Δg_{ex} <0 (Figure 1D, dashed green line) and there is an added energy penalty associated with nucleation through their aggregation. The impact of cluster aggregation for positive Δg_{ex} is illustrated in Figure 1C.

Beyond inducing changes in the magnitude of the barrier, the second effect of these features in the free energy landscape is that the relationship between the barrier (or rate) and the supersaturation deviates from the simple α^3/σ^2 dependence seen in Eqn. S2 and S3. Even in the case of a simple size dependence, such as the exponential rise described above, the resulting relationship is complex. In the case of cluster aggregation in an otherwise flat landscape, if we write $\Delta g_{ex} = 4\pi r_{Cl}^2\alpha_{Cl}$, where α_{Cl} is the effective interfacial energy of a cluster, then in Eqn. S3 σ is simply replaced by:

$$\sigma' = \sigma + \frac{3\Omega\alpha_{Cl}}{r_{Cl}\mathbf{k}T} \qquad \text{(S7)}$$

In the case where the minimum is global, there is a stable population of clusters with a narrow size distribution and the plus sign in Eqn. S7 is replaced with a minus sign. For $r_{cl} \geq 0.5$ nm, $\alpha_{Cl} \leq 0.5\alpha$ and $\sigma \geq 4.5$, Eqn. S7 gives $\frac{\sigma' - \sigma}{\sigma} < 0.1$. Consequently, for the range of concentrations examined in this study, deviations from α^3/σ^2 due to cluster aggregation are unlikely to be observed.

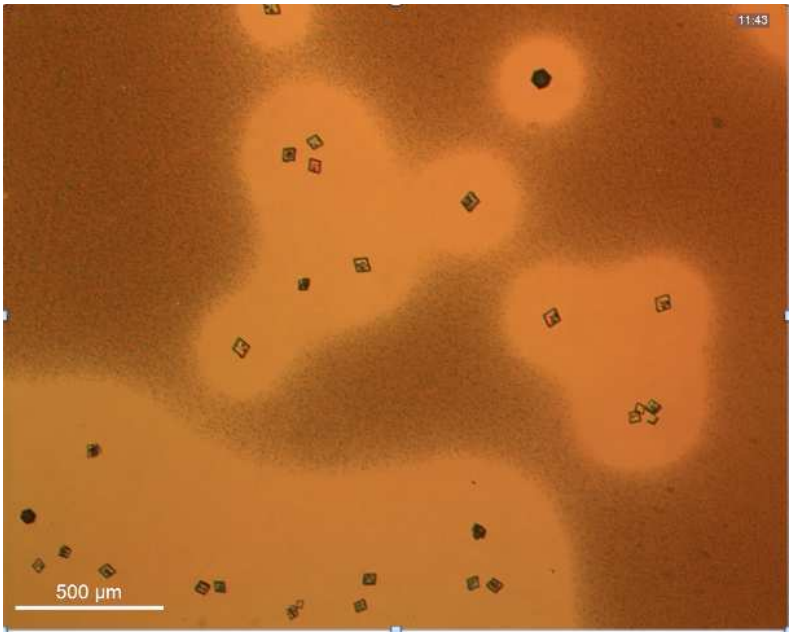

Movie S1 – Formation of ACC film on OH-terminated SAM followed by nucleation of calcite rhombs, which grow as the ACC film dissolves.

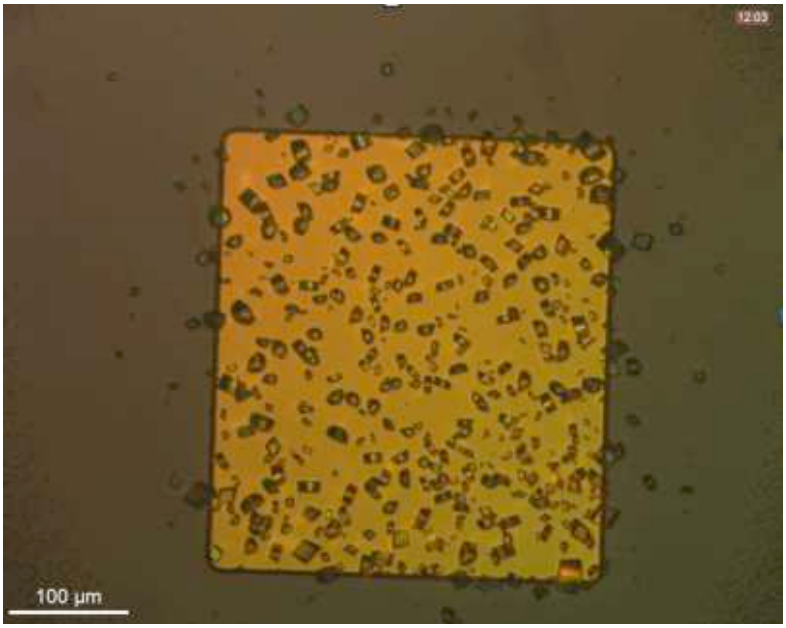

Movie S2 – Apparent direct formation of calcite on carboxyl-terminated SAM (MHA) under same conditions used for **Movie S1**.

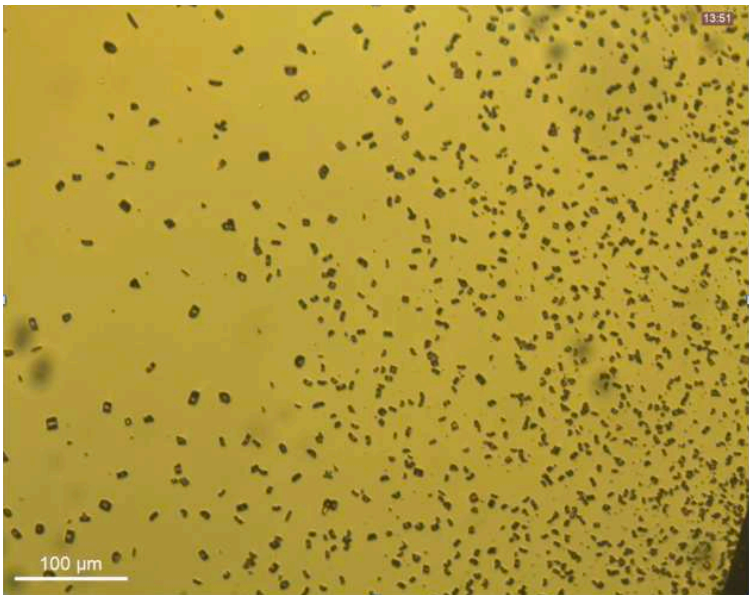

Movie S3 – Apparent direct formation of calcite on carboxyl-terminated SAM (MHA) under same conditions used for **Movie S2.** With the large SAM area, no ACC forms because the formation of calcite across the entire surface prevents the supersaturation from reaching the required level.

References

1. Lee, J.R.I., et al., *J. Am. Chem. Soc.*, 2007. **129**, 10370-10381.
2. Allison, J.D., D.S. Brown, and K.J. Novo-Gradac, *MINTEQA2/PRODEFA2, a geochemical assessment model for environmental systems: Version 3. 0 user's manual*, in *US Environmental Protection Agency, Athens, GA*. 1991. p. 117
3. Brecevic, L. and A.E. Nielsen, *J. Cryst. Growth*, 1989, **98**, 504-510.
4. Aizenberg, J., A.J. Black, and G.M. Whitesides, *J. Am. Chem. Soc.*, 1999, **121**, 4500-4509.
5 Smith, W., *J. Mol. Graphics*, 1996, **14**, 136-141.
6 Duffy, D.M., *Langmuir*, **20**, 2004, 7637-7642.
7 Quigley, D., *J. Chem. Phys*., 2009, **131**, 094703.
8 Moller, M.A., *J. Chem. Phys.*, 1991, **94**, 8390-8401.
9 MacKerell, A., *J. Phys. Chem.*, 1998, **B 102**, 3586-3616.
10 Jorgensen, W.L., *J. Chem. Phys*., 1983, **79**, 926-935.
11 Pavese, A., *Phys. Chem. Miner*., 1992, **19**, 80-87.
12 Pavese, A., *Phys. Chem. Miner*., 1992, **23**, 89-93.
13 Schroder, K.-P., *Chem. Phys. Lett*., 1992, **188**, 320-325.
14 Freeman, C.L., *J. Phys. Chem.*, 2007, **C 111**, 11943-11951.
15 Duffy, D.M., *Langmuir*, 2004, **20**, 7630-7636.
16. De Yoreo, J.J. and P.G. Vekilov, *Reviews in Mineralogy and Geochemistry*, 2003, **54**, 57-93.
17. Rull Perez, F., and Martinez-Frias, J., *J. Raman Spectroscopy*, 2003, **34**, 367-370.
18. Urmos, J., Sharma, S.K., and Mackenzie, F.T., *Amer. Min*., 1991, **76**, 641-646.
19. Addadi, L., Raz, S., and Weiner, S., Adv. Mater., 2003, **15**, 959-970.
20. Raz, S., Testeniere, O., Hecker, A., Weiner, S., and Luquet, G. *Biol Bull.*, 2002, **203**, 269-274.
21. Davis, K.J., Dove, P.M. and De Yoreo, J.J., *Science,* 2000, **290,** 1134-1137.